**Enhancing inter-domain connectivity by reducing fractal dimension: the key to passivating deep traps in organic photovoltaics**

Yuang Fu, ‡ a Luhang Xu, ‡ a Yuhao Li, ‡ abc Emily J. Yang,d Yu Guo,e Guilong Cai,af Pok Fung Chan,a Yubin Ke,*bc Chun-Jen Su,g U-Ser Jeng,gh  Philip C. Y. Chow,e Ji-Seon Kim,d Man-Chung Tang,*i Xinhui Lu*a

a Department of Physics, The Chinese University of Hong Kong, New Territories, Hong Kong 999077, China.

b Spallation Neutron Source Science Centre, Dongguan 523803, China.

c Institute of High Energy Physics, Chinese Academy of Sciences, Beijing 10049, China.

d Department of Physics and Centre for Processable Electronics, Imperial College London, Blackett Laboratory, London, SW7 2AZ UK.

e Beijing Key Laboratory of Ionic Liquids Clean Process, Institute of Process Engineering, Chinese Academy of Sciences, Beijing, China.

f National Synchrotron Radiation Research Centre, 101 Hsin-Ann Road, Science-Based Industrial Park, Hsinchu 30077, Taiwan.

g Department of Chemical Engineering & College of Semiconductor Research, National Tsing Hua University, Hsinchu 300044, Taiwan.

h Institute of Materials Research, Tsinghua Shenzhen International Graduate School, Tsinghua University, Shenzhen 518055, China.

‡ Y.F., L.X., and Y.L. contributed equally to this work.

# Experimental Methods

*Materials:* Chloroform (99.5%), chlorobenzene (99.8%), 1-chloronapthalene (96.0%), and 1,4-diiodobenzene (DIB) (99.0%) were purchased from Sigma-Aldrich. PM6 and Y6 were purchased from Solarmer Inc (Beijing). D18 and L8BO were purchased from Derthon Optoelectronic Materials Science Technology Co LTD. PNDIT-F3N was purchased from eFlexPV Ltd. PEDOT:PSS (Clevios P VP AI 4083) was purchased from Heraeus Ltd. Unless stated otherwise, all solvents and reagents were used as received without further purification.

***Device fabrication and characterisation:*** All the devices were fabricated based on a conventional sandwich structure of patterned ITO glass/PEDOT:PSS/active layer/PNDIT-F3N/Ag. The ITO substrates were sonicated for 20 mins using detergent, deionised water, acetone, and isopropanol consecutively before being treated with UV-ozone for 20 min. PEDOT:PSS was spin-cast onto the ITO substrates at 4000 rpm for 30 s and then dried at 120 °C for 20 min in air. The substrates were then transferred into a glovebox filled with $N_2$, where active layers (1:1.2 wt%) were deposited. For BHJ devices, the active layer materials were dissolved in different solvents (15.4 mg/ml in CF with 0.5 vol% CN or 10 mg/ml DIB, 20 mg/ml in CB with 0.5 vol% CN ) and stirred at 40 °C, 300 rpm for 2 hours before use. The active layer was deposited at 3000 rpm for 30 s, followed by thermal annealing at 100 °C for 5 mins. For BHJ-AC, active layer materials were dissolved in CF without additives and thermal annealing. For LBL devices, all precursor solutions were stirred at 40 °C, 300 rpm for 2 hours apart from D18 solution, which was stirred at 100 °C for 2 hours and cooled down to 60 °C 5 mins before use. PM6 solution (7 mg/ml in CF) was deposited at 2300 rpm for 30 s. D18 (4 mg/ml in CF) was deposited at 2500 rpm for 30 s. All donor layers were thermally annealed at 100 °C for 10 mins after casting. Y6 solution (8.4 mg/ml in CF) or L8BO solution (7.5 mg/ml in CF) was then deposited at 2500 rpm for 30 s, followed by thermal annealing at 100 °C for 5 mins. Various additives (CN and DIB) were added to the acceptor precursor solution only. PNDIT-F3N (0.5 mg/ml in ethanol, with 0.5 vol% ethanoic acid) was deposited at 2000 rpm for 30 s, followed by thermal evaporation of Ag electrode (100 nm) at $< 10^{-4}$ Pa.

The current density-voltage (*J-V*) curves of devices were measured using a Keithley 2400 Source Meter (-0.2 V-1.2 V, forward scan, 10 mV per step, 10 ms dwell time) in a nitrogen-filled glove box under AM 1.5G (100 mW cm$^{-2}$) illumination using a solar simulator (SS-F5-3A, Enlitech). The intensity of the light source was calibrated by a reference silicon solar cell (SRC2020, Enlitech). The device area was determined by the overlap between the top and bottom electrodes, which was 0.0439 cm$^{-2}$, as confirmed by the optical microscope. The external quantum efficiency (EQE) was measured by a QE/IPCE system (Enli Technology Co. Ltd. China) in a wavelength range of 300-1000 nm, 5 nm per step. For $J_{ph}$-$V_{eff}$ measurements, dark and light currents ($J_{light}$ and $J_{dark}$) were measured under the range of -2 V-1.2 V, 50 meV per step, so that $J_{ph}$ can be derived as $J_{ph} = J_{dark}$- $J_{light}$. The bias applied to the

active layer, $V_{cor}$, can be obtained from the equation $V_{cor}=V-J_{light} \times R_s$ where $R_s$ is the series resistance of the device derived from the differential resistance of dark $J$-$V$ curve under the forward bias of 1.2 V.

***Optical characterisations:*** The absorption spectra of thin films were measured using Perkin Elmer Lambda 950 UV/Vis/IR with wavelength scanned from 1000 nm to 300 nm, 1 nm per step. The Resonant Raman spectra of neat Y6 films were measured using the Renishaw inVia Raman microscope using an excitation wavelength of 633 nm. For both measurements, samples were deposited on quartz substrates.

***DFT simulations:*** Density functional theory (DFT) calculations were performed using Gaussian 16 software[1] on the Imperial College High-Performance Computing service, and results were visualised using GaussView 6.0.17. The optimised ground state geometry and simulated Raman spectra of single, gas phase molecules were calculated using the DFT method at the B3LYP (hybrid) level of theory with the 6-311G(d,p) basis set,[2] with an empirical scaling factor of 0.97 applied to Raman peak wavenumbers.[3] Dihedral scans were performed by optimising the molecular structure with a frozen dihedral coordinate before calculating the simulated Raman spectra at each angle to understand the spectral changes associated with twisting in the BT core unit.

***AFM and c-AFM measurements:*** JPK NanoWizard NanoOptics atomic force microscope (AFM) with a Tap300Al-G tip (40 N/m) was used for topography and phase characterisations of neat and blend films. Measurements were performed using tapping mode with the tip oscillating at a fixed frequency (~300 kHz) and an amplitude above the sample surface. c-AFM measurements were conducted using an ElectriCont-G tip (0.2 N/m, coated with Pt/Ir) in contact mode. A positive bias was applied to the sample substrate so that holes could be injected from PEDOT:PSS to the active layer before getting collected by the tip, which was recorded as a negative current flow. Considering the relatively flat surfaces of all films studied, the current contrast in c-AFM mappings mainly arises from the HOMO offset between PM6 and Y6-rich domains resulting in different injection barriers.[4-6] The scale bars in all the c-AFM figures (**Figure 2d-f**) have been adjusted so that the bright phases are low-current regions, corresponding to Y6-rich phases with a larger injection barrier for PEDOT:PSS. For both AFM and c-AFM measurements, the tip scanned over 256 pixels across a 2 μm range at a scan rate of 1 Hz. A 2×2 μm image was obtained for each sample. The root-mean-square (RMS) fluctuations in height and current were obtained using the JPKSPM Data Processing software package.

***GIWAXS, GISAXS, GISANS measurements and fittings:*** GIWAXS measurements for neat and blend films, and GISAXS measurements for neat films were carried out with a Xeuss 2.0 SAXS/WAXS laboratory beamline using a Cu X-ray source (8.05 keV, 1.54 Å) and a Pilatus3R 300 K detector.[7, 8] The incidence angle was 0.15. GISAXS measurements for blend films were conducted at 23A SWAXS beamline at the National Synchrotron Radiation Research Center, Hsinchu, Taiwan, using a 10 keV

primary beam, 0.15° incident angle, and Pilatus 1M-F and C9728DK area detector. GISANS measurements were conducted at BL-01 (SANS) beamline at the China Spallation Neutron Source (CSNS). All the samples were spin-coated on the UV-ozone-treated silicon substrates.

The GISAXS and GISANS profiles were fitted using the general **equation 1**:

$$I(q) = \frac{A_1}{[1+(q\xi)^2]^2} + A_2 \langle P(q,R_{gc}) \rangle S_{frac}(q,R_{gc},\eta,D_f) + A_3 \langle P(q,R_{gc}) \rangle S_{hs}(q,R_{gc},\Phi) + A_4 \tag{1}$$

where $q$ is the scattering vector. The amorphous intermixed region was fitted using the Debye−Anderson−Brumberger (DAB) model (the 1st term)[9] with perfector $A_1$ and correlation length $\xi$. The crystalline Y6 domains were fitted using spherical form factor $P(q,R_{gc})$ multiplied by either a fractal[10] (the 2nd term ) or a hard-sphere[11] structure factor (the 3rd term) with domain size represented by twice the radius of gyration $2R_{gc}$. The 4th term represents the incoherent background scattering. GISAXS profiles of CF-processed PM6:Y6 and D18:L8BO films were fitted using the sum of the 1st, the 2nd, and the 4th terms. The GISAXS profile of BHJ-CB (PM6:Y6) film was fitted using the 1st, the 3rd, and the 4th terms. The GISANS profiles were fitted using the sum of the 2nd, the 3rd and the 4th terms.

*Voltage-dependent capacitance spectroscopy:* All devices were encapsulated and tested in air. A 10 meV AC bias was applied to the device with frequency scanning from 4 MHz to 10 kHz, and the corresponding AC current was measured to obtain the complex impedance of the device as a function of frequency. The total capacitance ($C_{cor}$) of the device was derived from the complex impedance using **equation 2**, excluding the effect of series resistance ($R_s$) and parasitic inductance ($L_I$).[12, 13]

$$C_{cor} = -\frac{1}{\omega}\left[\frac{Z'' - \omega L_I}{(Z' - R_s)^2 + (Z'' - \omega L_I)^2}\right] \tag{2}$$

where $Z'$ and $Z''$ are the real and imaginary parts of the complex impedance, respectively, and $\omega$ is the angular frequency. After subtracting the $C_{cor}$ by the geometric capacitance ($C_g$, measured under dark at -1 V), the total capacitance associated with the active layer only ($C_T$) was obtained, and the chemical capacitance ($C_\mu$) was derived from the saturated $C_T$ at low frequency. Measurements were carried out with devices under 1 sun-equivalent LED illumination and constant background bias ($V_{DC}$) scanning from −1 to 0.9 V and -1 to 1 V for PM6:Y6 and D18:L8BO devices, respectively (**Figure S3a-c**). Charge carrier density within the active layer ($n$, see **Figure S3d-f**) was obtained by integrating the $C_\mu$ with respect to the corrected applied bias ($V_{cor}= V_{app}-JR_s$) using **equations 3** and **4**

$$n(V_{cor}) = n_{sat} + \frac{1}{qAL}\int_{V_{sat}}^{V_{cor}} C_\mu dV_{cor} \tag{3}$$

$$n_{sat} = \frac{1}{qAL}C_{sat}(V_0 - V_{sat}) \tag{4}$$

where $C_{sat}$ is the saturated $C_\mu$ measured at $V_{sat}$ (−1V) under 1 sun. $V_0$ is the forward bias at which $J_{ph}$

equals 0. $L$ is the thickness of the active layer (around 100 nm). Effective charge carrier mobilities ($\mu_{eff}$) at various $V_{cor}$ (see **Figure S3g-i**) were obtained via **equation 5**.[14]

$$\mu_{eff}(n, V_{cor}) = \frac{J(V_{cor}) \cdot L}{2qn(V_{cor}) \cdot [V_{cor} - V_{oc}]}$$

(5)

With those results, we then fitted $J_{rec}$ as a function of $V_{cor}$ using the linear superposition of bimolecular ($J_{br}$) and bulk trap-assisted recombination (Jtb )currents, as shown in equations **6** and **7**.

$$J_{br} = qLk_{bm}n^2 = \frac{2q^2L}{\varepsilon_0\varepsilon_r}\gamma\mu_{eff}n^2$$

(6)

$$J_{tb} = qLk_{tb}n = \frac{q^2L}{\varepsilon_0\varepsilon_r}\mu_{eff}N_{tb}n$$

(7)

where $q$ is the elementary charge, $\varepsilon_0$ and $\varepsilon_r$ are the permittivity of free space and dielectric constant, respectively. The Langevin reduction factor $\gamma$ for bimolecular recombination and the bulk trap density $N_{tb}$ were left as fitting parameters. All curves could be fitted without involving surface recombination current, which is reasonable considering that both charge transport layers used (PEDOT:PSS and F3N) have been shown to exhibit good carrier selectivity for the PM6:Y6 system.[15] These results are summarised in **Figure 1**, **S14**, and **S28**.

**Supplementary Note**

**Supplementary Note 1 Domain size and exciton dissociation in NFA blend films**

The apparent domain size we extracted from GISAXS fitting is $2R_{gc}$, where $R_{gc}$ stands for the radius of gyration. For polymer:fullerene blend films, the scattering contribution from fullerene agglomerates was typically fitted using a spherical form factor multiplied by a hard-sphere structure factor.[9] In this case, $R_{gc}$ is directly proportional to the radius of closely packed fullerene agglomerates, so $2R_{gc}$ must not exceed the exciton diffusion length for efficient exciton dissociation to take place.[11] In contrast, NFAs with anisotropic molecular structures form fractal networks in blend films with space-filling properties described by the fractal dimension.[16] In particular, LBL-DIB has a reduced fractal dimension of 2, which means Y6 crystalline domains form extended interpenetrating networks with PM6 rather than densely packed agglomerates. In this case, the previous conclusion based on fullerene acceptors may no longer apply.

As shown in **Figure S7a** and **b,** the timescales for the diffusion-limited hole transfer process become longer in DIB-processed films than in CN-processed films (11.2 ps v.s. 16.1 ps and 13.7 ps v.s. 21.2 ps for BHJ and LBL films, respectively). Nonetheless, exciton dissociation yield should approach unity in all four systems due to the much longer exciton lifetime (>1 ns) of Y6.[17, 18]

Assuming all films have similar exciton diffusion coefficients, the magnitude of $\tau_2$ reflects the size of Y6 crystalline domains. However, taking LBL-CN and LBL-DIB as an example, the difference in $\tau_2$ (13.7 ps v.s. 21.2 ps) is much smaller than the difference in $2R_{gc}$s extracted from GISAXS fittings (17.2 nm v.s. 74.1 nm). This is because Y6 forms an extended interpenetrating network (characterised by a low fractal dimension) in LBL-DIB. As a result, there should be abundant D:A interface for exciton dissociation to take place even though the 'apparent domain size' ($2R_{gc}$s) exceeds the exciton diffusion length (30-40 nm).[19]

# Supplementary Figures
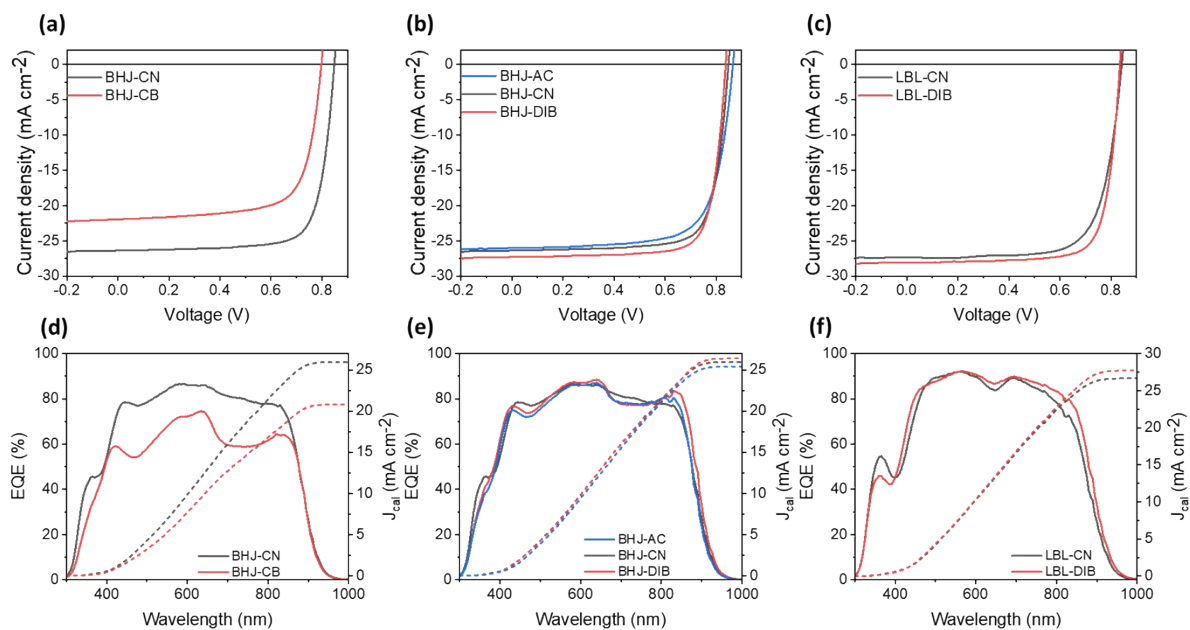


**Figure S1.** *J-V* curves for PM6:Y6 devices processed with different **a** solvents and **b** additives for BHJ and **c** LBL devices. The corresponding external quantum efficiency (*EQE*) curves (solid lines) with their corresponding *J*$_{sc}$ calculated (*J*$_{cal}$, dotted lines) are shown in **d-f**.
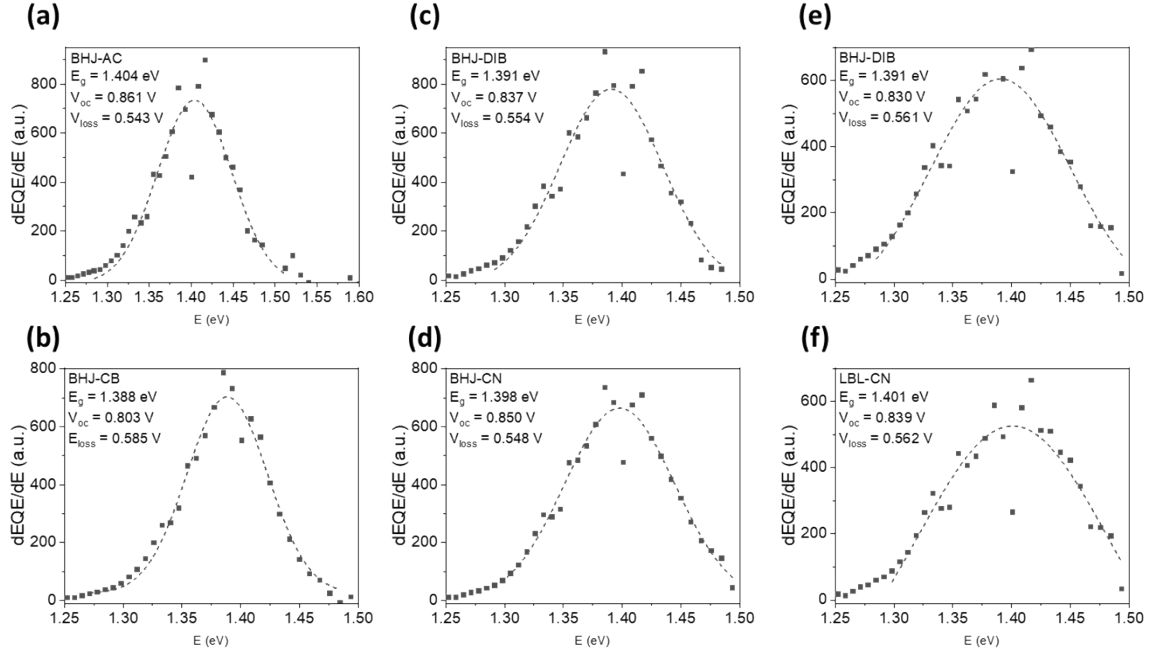
**Figure S2.** The photovoltaic bandgap ($E_{gPV}$) determined from the peak of d$EQE$/d$E$[20, 21] for PM6:Y6 devices processed under different conditions. $V_{oc}$ loss ($V_{loss}$) was determined as the difference between $E_{gPV}$ and the average $V_{oc}$.
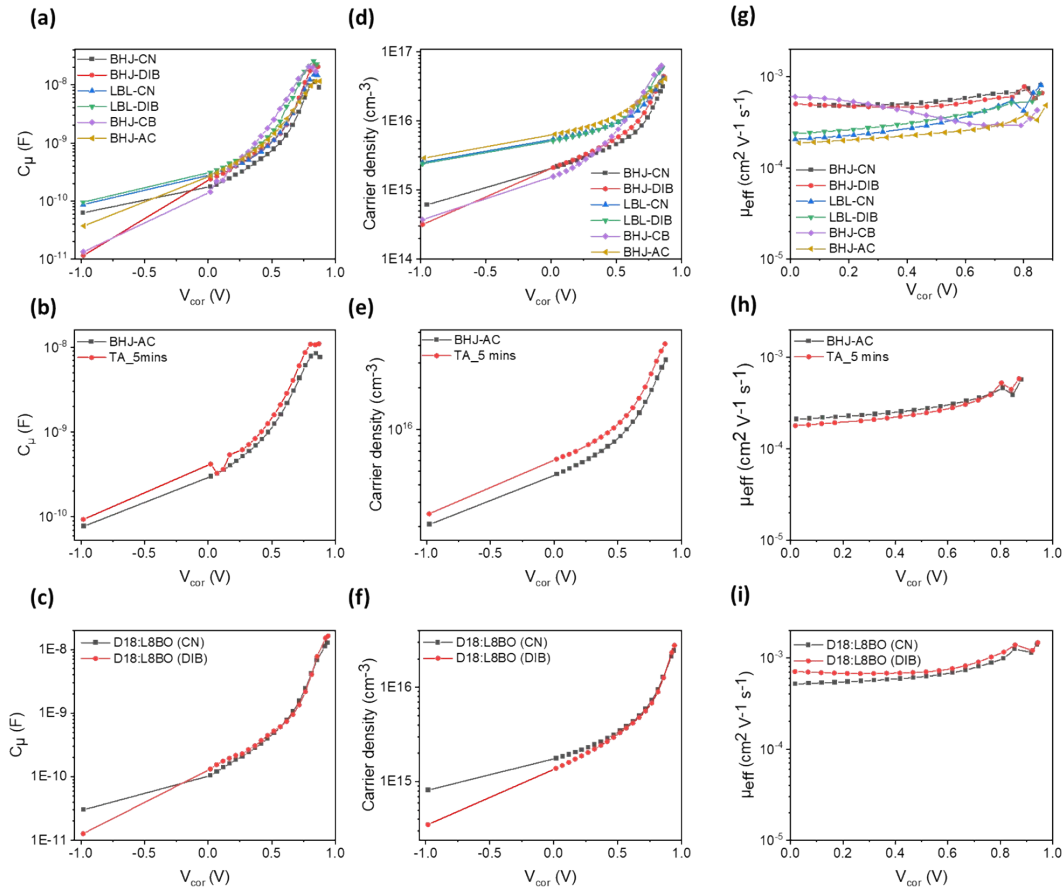


**Figure S3. a-c** Chemical capacitance ($C_\mu$) and **d-f** Charge carrier density stored within the active layer

of devices as a function of corrected bias ($V_{cor} = V\text{-}JR_s$). All devices were measured under 1-sun-equivalent white LED illumination. **g-i** Effective mobility ($\mu_{eff}$) as a function of $V_{cor}$. It is linked to both electron ($\mu_e$) and hole ($\mu_h$) mobilities via the equation $\mu_{eff} = \dfrac{2\mu_e\mu_h}{\mu_e + \mu_h}$.
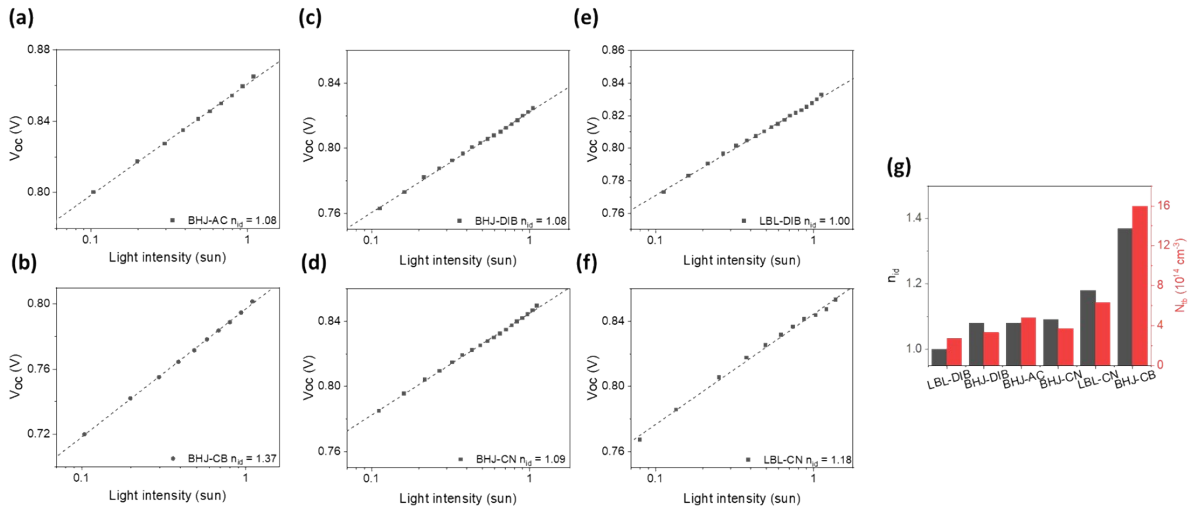


**Figure S4. a-f** Light intensity-dependent $V_{oc}$ measurements for PM6:Y6 devices fabricated under different conditions. For each figure, the ideality factor ($n_{id}$) extracted from the slope is shown in the inset. A comparison between $n_{id}$ and $N_{tb}$ extracted from capacitance spectroscopy measurements is summarised in **g**. The non-ideal positive correlation between $n_{id}$ and $N_{tb}$ can be understood from the fact that the magnitude of $n_{id}$ depends on the relative extent of bimolecular and trap-assisted recombination, which not only depends on $N_{tb}$, but also on $\gamma$ and charge carrier density.[22]
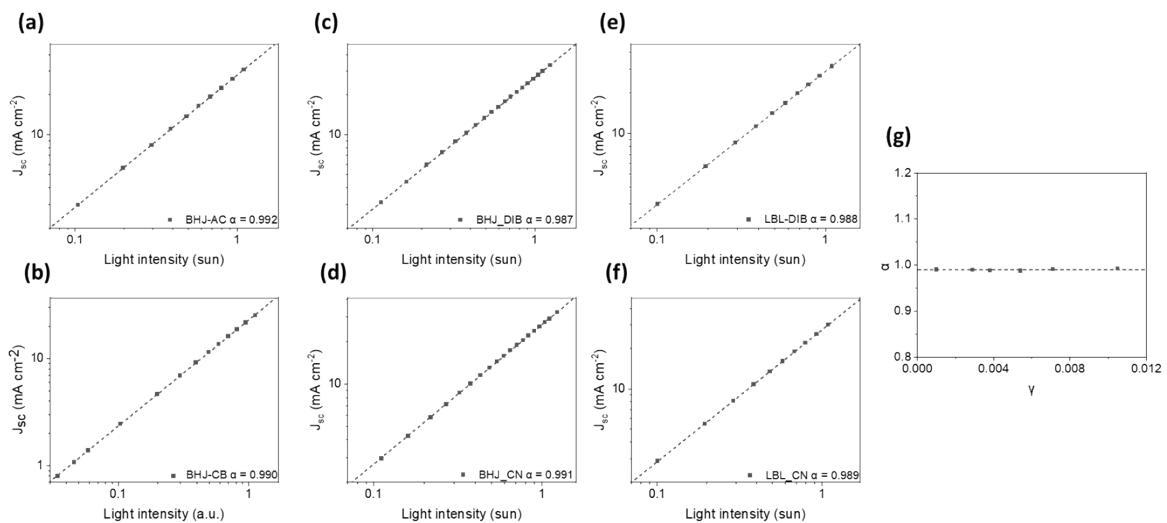


**Figure S5. a-f** Light intensity-dependent $J_{sc}$ measurements for PM6:Y6 devices fabricated under

different conditions. For each figure, the power law exponent ($\alpha$) extracted from the slope is shown in the inset. There is a lack of correlation between $\alpha$ and $\gamma$, as shown in **g**. It can be attributed to the suppressed bimolecular recombination and efficient charge extraction in all PM6:Y6 devices so that the deviation onset of $\alpha$ does not readily occur within the light intensity range employed in this measurement.[23]
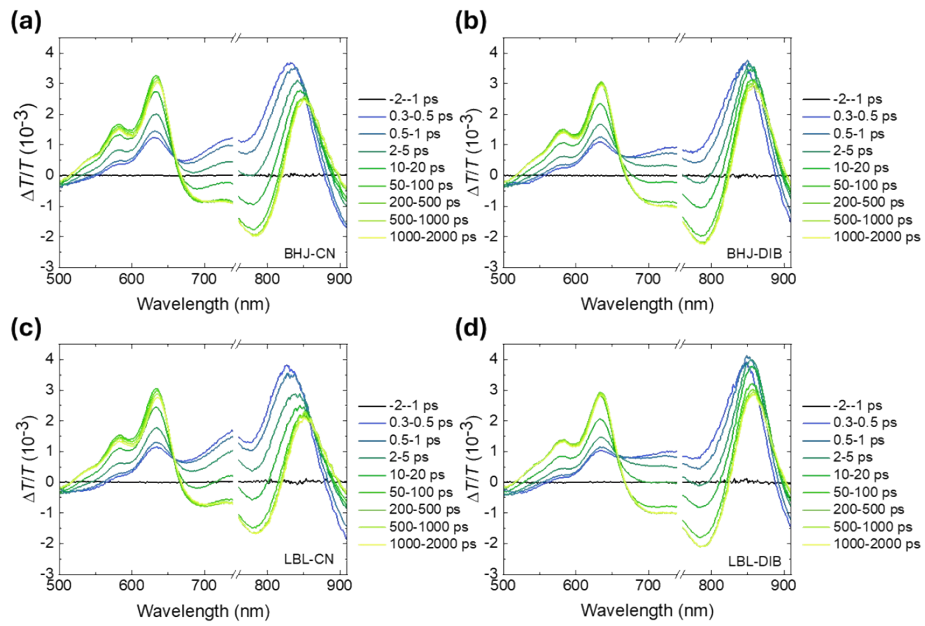
**Figure S6.** Transient absorption spectra of **a** BHJ-CN, **b** BHJ-DIB, **c** LBL-CN, and **d** LBL-DIB. The excitation wavelength was chosen to be 750 nm with a fluence of 4.5 μJ cm$^{-2}$ for selective excitation of Y6.
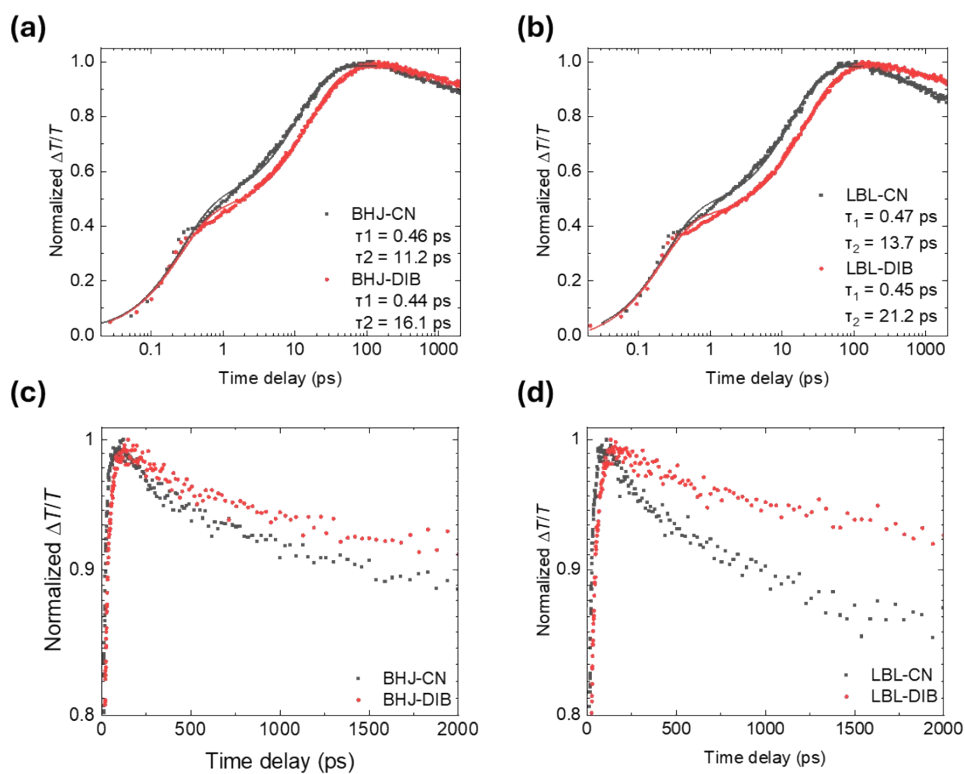


**Figure S7.** Time evolutions of the transient absorption signals monitored at 610-650 nm (PM6 GSB) for **a** BHJ-CN, BHJ-DIB and **b** LBL-CN, LBL-DIB (dots). The growth kinetics are similar to previous reports in PM6:Y6 blend films.[24, 25] Each curve is fitted using a bi-exponential growth function (solid line) with $\tau_1$ and $\tau_2$ corresponding to the characteristic timescales for the interfacial and diffusion-limited hole transfer processes, respectively. The corresponding plots with the x-axis adjusted to linear scale are presented in **c** and **d** to show the difference in recombination kinetics after 100 ps. We note that due to efficient free charge generation in PM6:Y6 blend films, the decay kinetics should contain contributions from both geminate and non-geminate recombination under the excitation fluence we employed (4.5 μJ cm$^{-2}$).[26, 27]
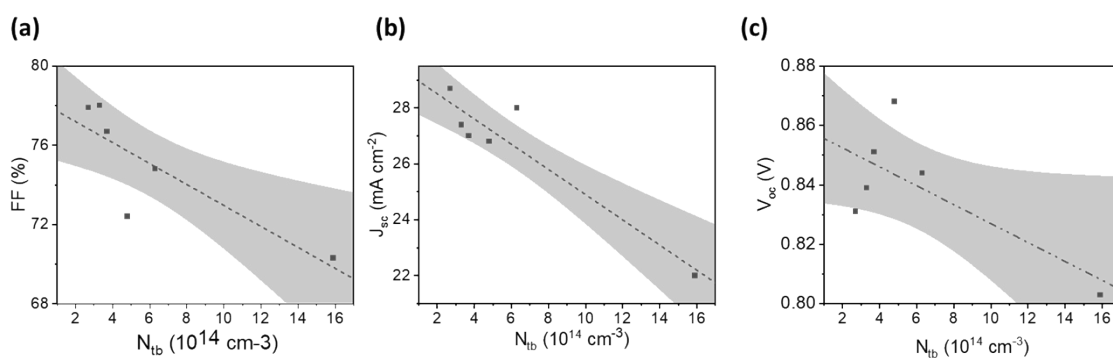
**Figure S8.** The impact of deep trap density ($N_{tb}$) on **a** *FF*, **b** $J_{sc}$, and **c** $V_{oc}$ of PM6:Y6 devices processed under different conditions. The 90 % confidence zone is shown as the grey shaded area.
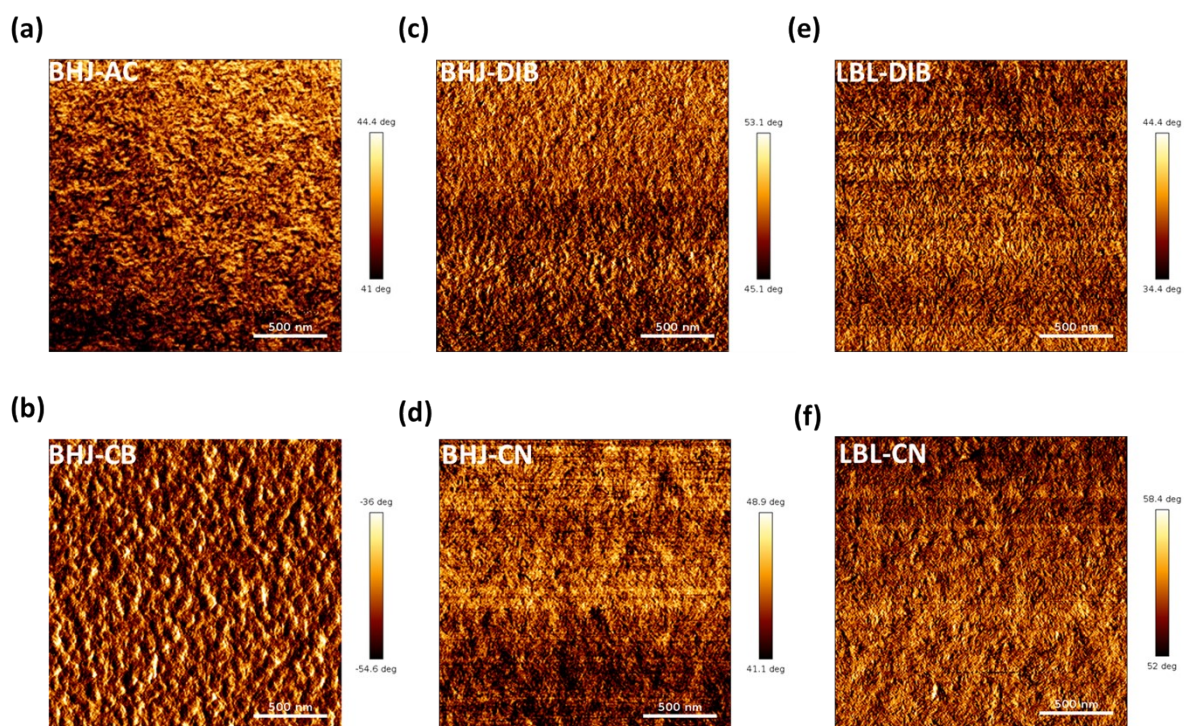


**Figure S9.** AFM phase mappings of PM6:Y6 blend films processed under different conditions.
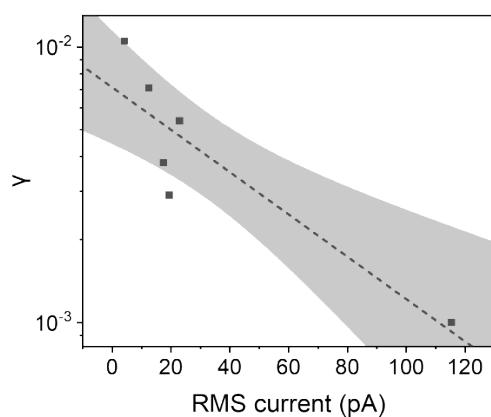
**Figure S10.** The inverse correlation between $\gamma$ obtained from capacitance spectroscopy measurements and RMS current fluctuation obtained from c-AFM measurements for PM6:Y6 devices fabricated under different conditions.
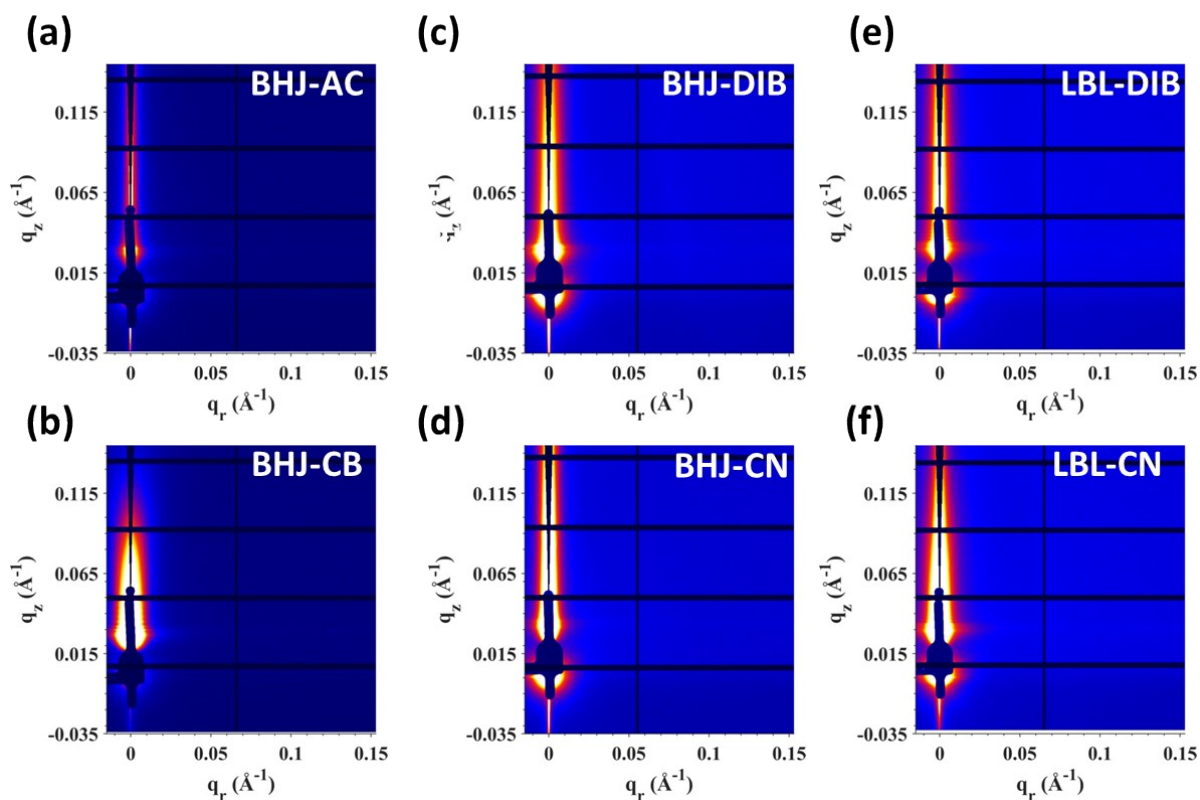


**Figure S11.** 2-D GISAXS plots of PM6:Y6 blend films processed under different conditions.
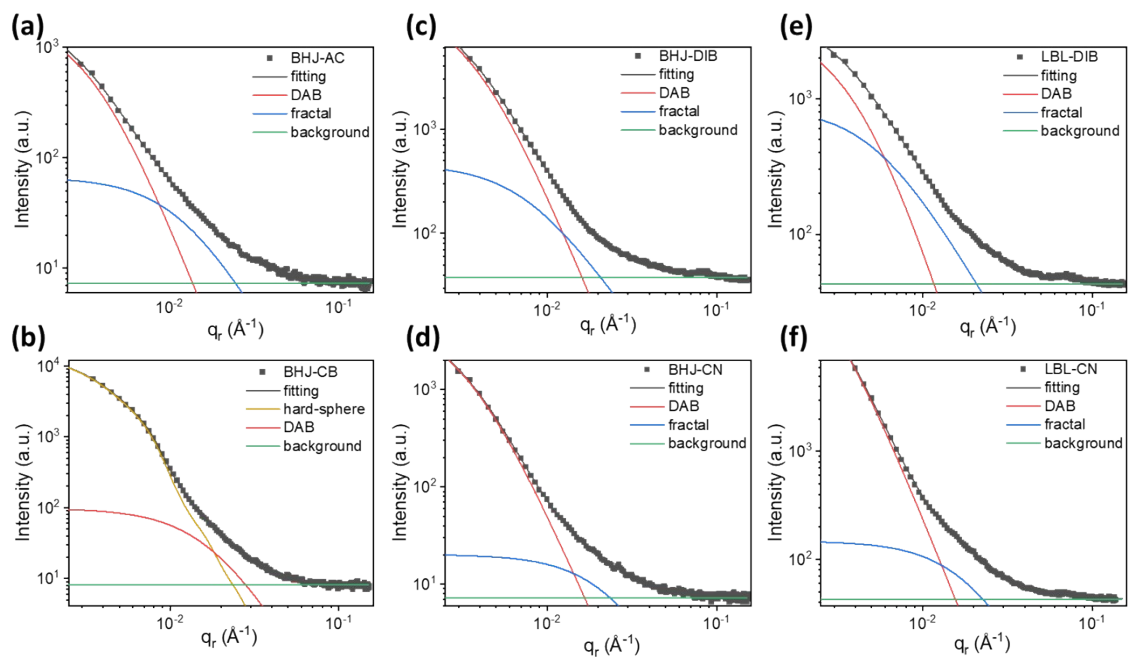
**Figure S12.** The in-plane GISAXS linecuts extracted at the Yoneda peak positions (dots) with their best fits (solid lines) for PM6:Y6 blend films processed under different conditions. The contribution from the DAB term (red), the fractal term (blue), the hard-sphere term (yellow), the background (green), and the over all fitting (black) were highlighted.
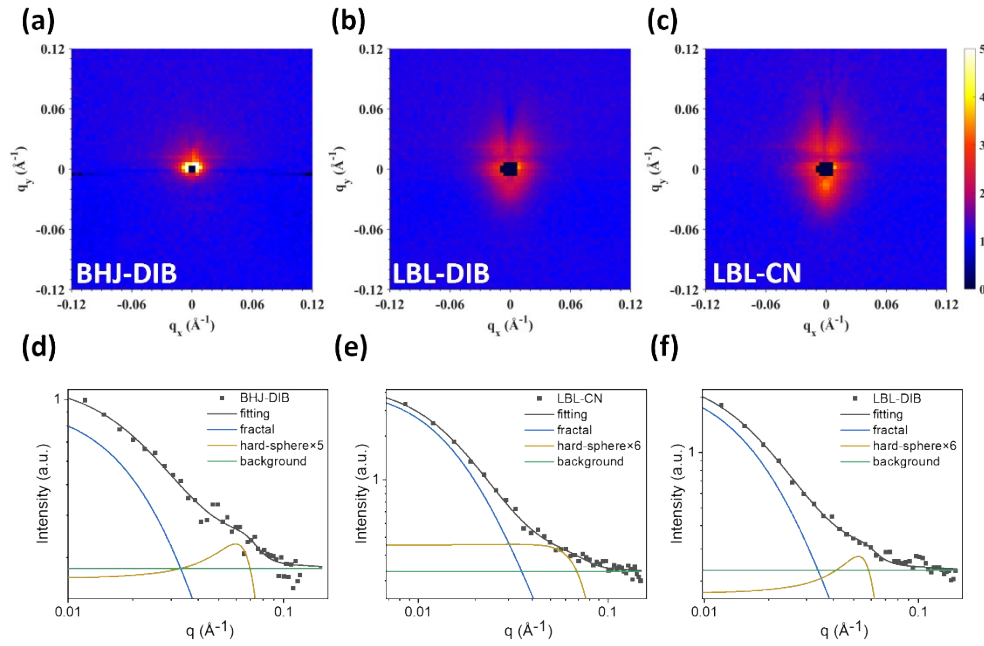
**Figure S13. (a)** 2-D GISANS plots of **(a)** BHJ-DIB, **(b)** LBL-CN and **(c)** LBL-DIB. The corresponding 1-D linecuts (dotted lines) extracted at the Yoneda peak positions and their best fits (solid lines) are shown in **d-f**.
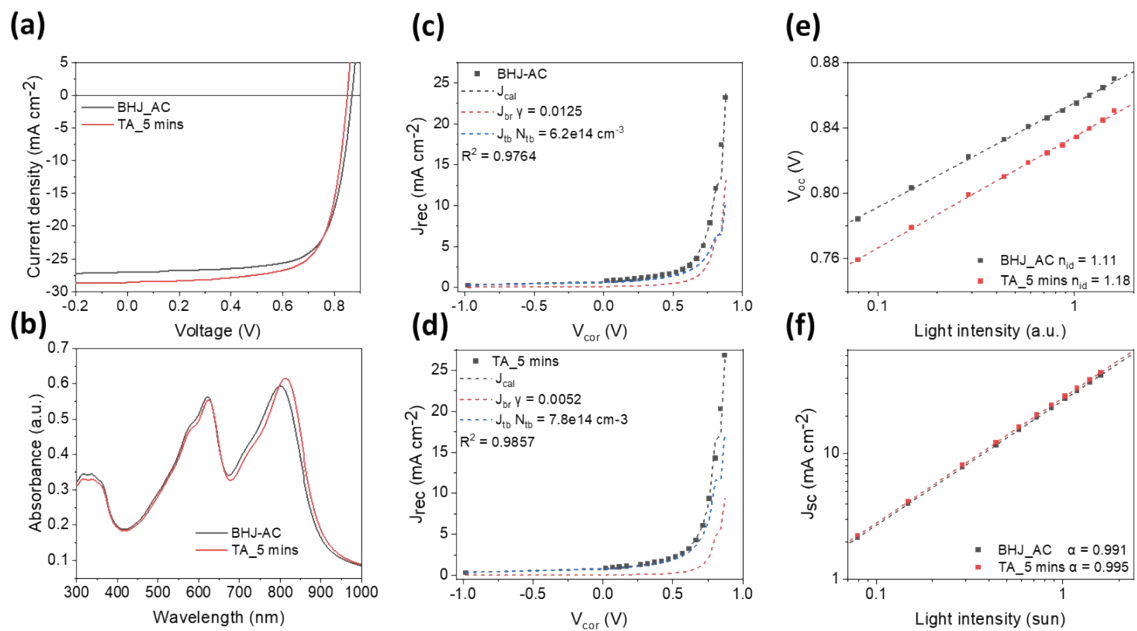


**Figure S14. a** Representative *J-V* curves comparing as-cast PM6:Y6 BHJ devices without (BHJ-AC) and with thermal annealing at 100 °C for 5 mins (TA_5 mins). The corresponding UV-Vis absorption spectra are shown in **b**. Recombination kinetics are compared in **c** and **d**, while the light-intensity-dependent *J-V* measurements are shown in **e** and **f**.
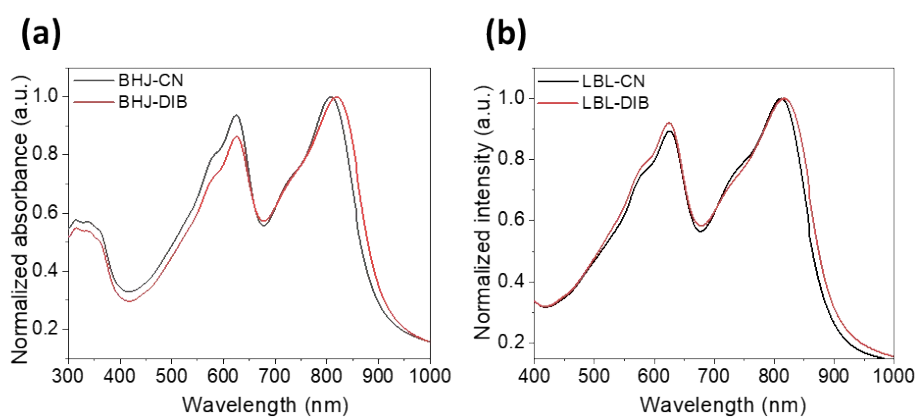
**Figure S15.** Normalized absorption spectra for PM6:Y6 **a** BHJ and **b** LBL films processed with CN and DIB. In both cases, DIB-processed films show red-shifted absorption peaks compared to CN-processed films. Additionally, compared to LBL-CN, LBL-DIB shows a more suppressed 0-1 shoulder relative to the main 0-0 peak.
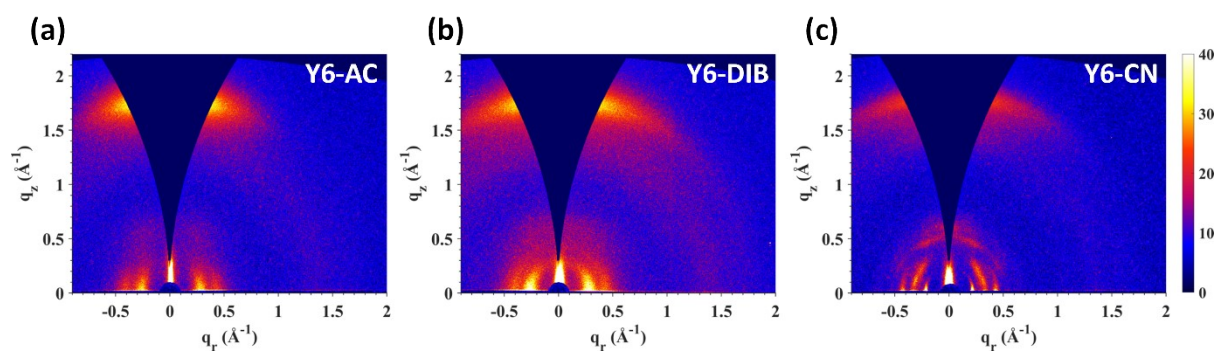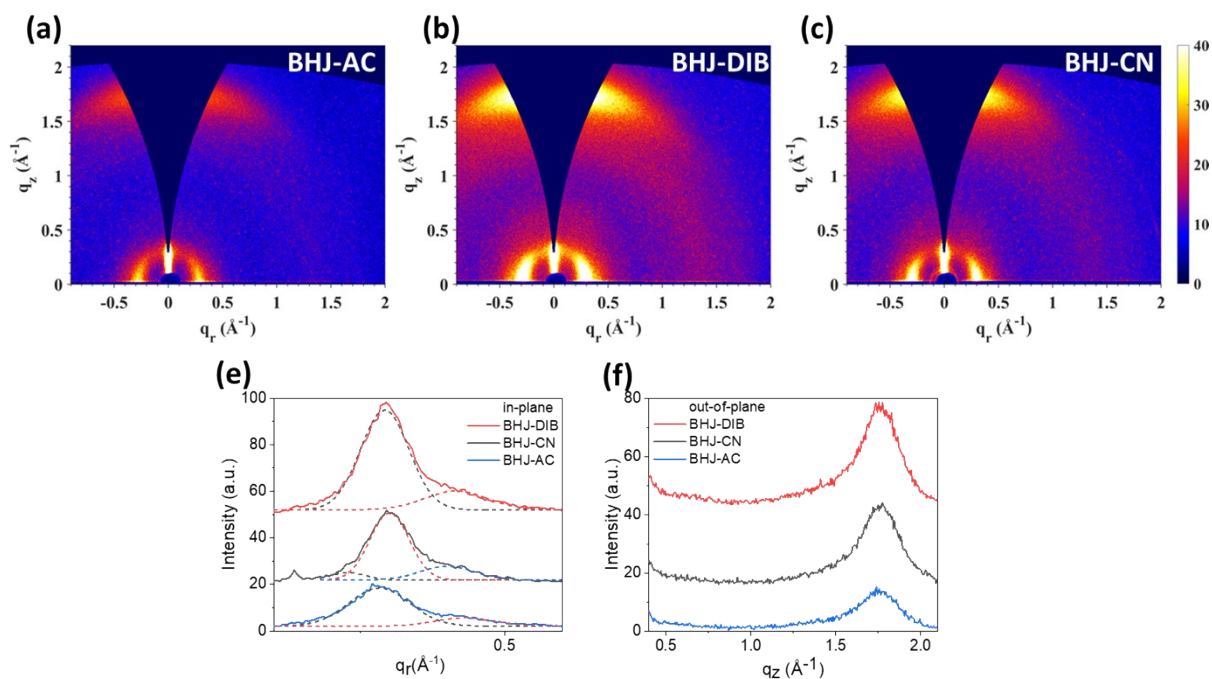


**Figure S16.** 2-D GIWAXS plots of neat Y6 films processed with different additives.
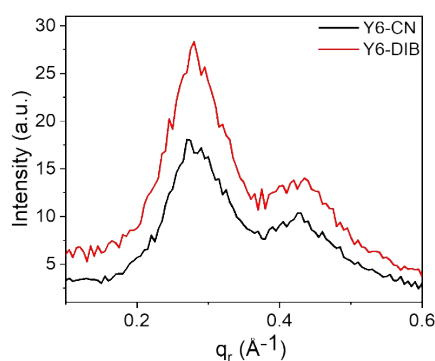


**Figure S17.** In-plane linecuts of Y6-AC and Y6-DIB in the small-q region. The y-axis is on the linear scale for better comparison.

**Figure S18.** 2-D GIWAXS plots of **a** BHJ-AC, **b** BHJ-DIB, and **c** BHJ-CN films with their corresponding linecuts along the in-plane and out-of-plane directions shown in **e** and **f**, respectively. The different Y6 packing structures between CN and DIB-processed films become less pronounced due to intermixing with PM6, but the triple peak along the in-plane direction is still identifiable for BHJ-CN, as shown in **e**.
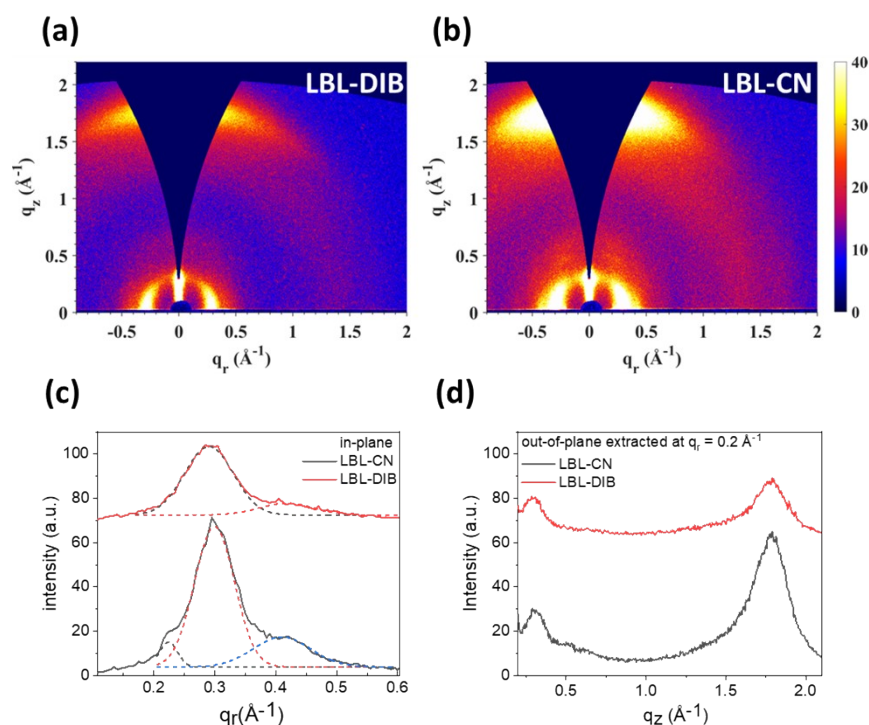
**Figure S19.** 2-D GIWAXS plots of **a** LBL-DIB and **b** LBL-CN films with their corresponding linecuts along the in-plane and out-of-plane directions shown in **c** and **d**, respectively. The pronounced triplet in-plane peaks exclusively observed in LBL-CN as well as the pronounced out-of-plane shoulder at 0.5-0.6 Å$^{-1}$ indicate that the distinct packing structures between Y6-CN and Y6-DIB are largely retained in LBL films.
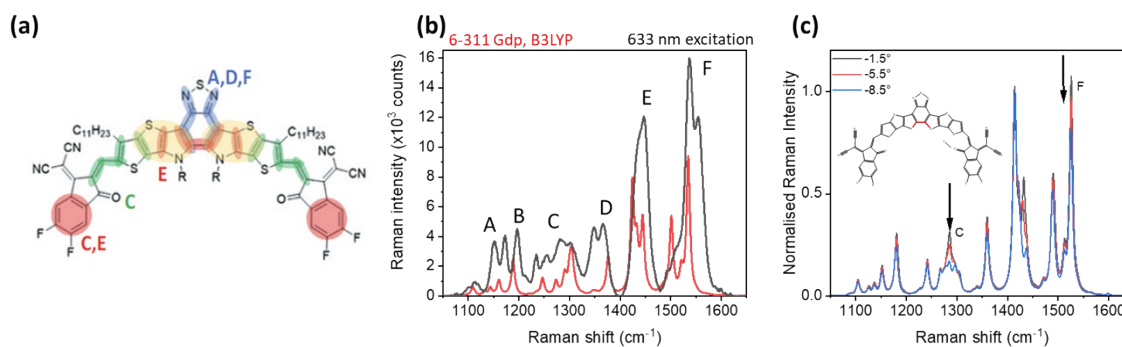


**Figure S20. a** The molecular structure of Y6 with different vibrational modes labelled. **b** Peak correlations between simulated and experimental Raman data. **c** Simulated Raman spectra showing selective quenching of peaks C and F with increasing dihedral angle on the BT core group. The bonds involved in the dihedral angle are highlighted in red at the inset. Side chains are omitted for clarity.
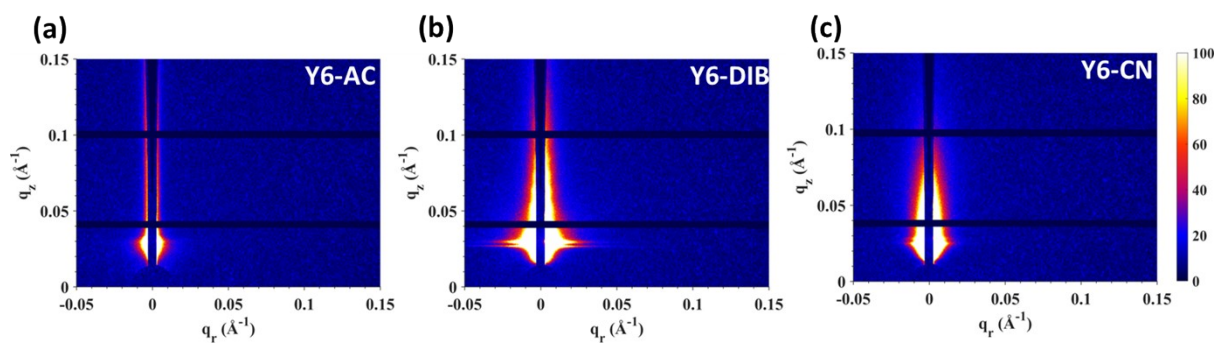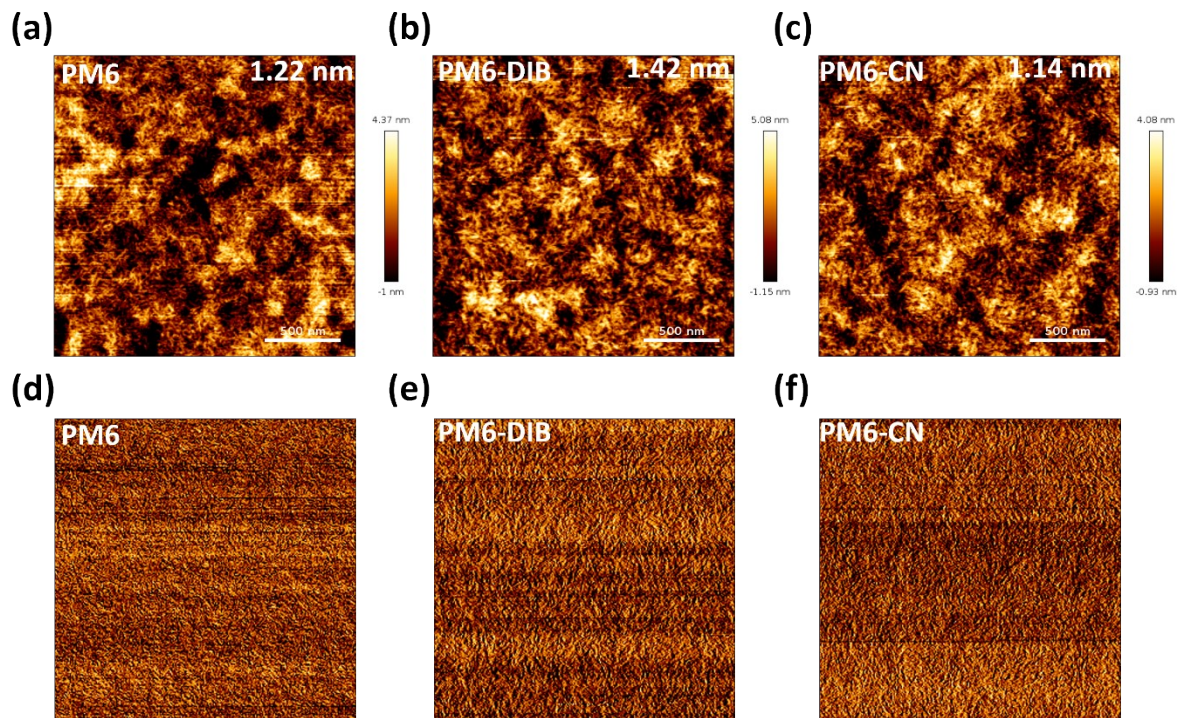
**Figure S21.** 2-D GISAXS plots of Y6 neat films processed under different conditions.
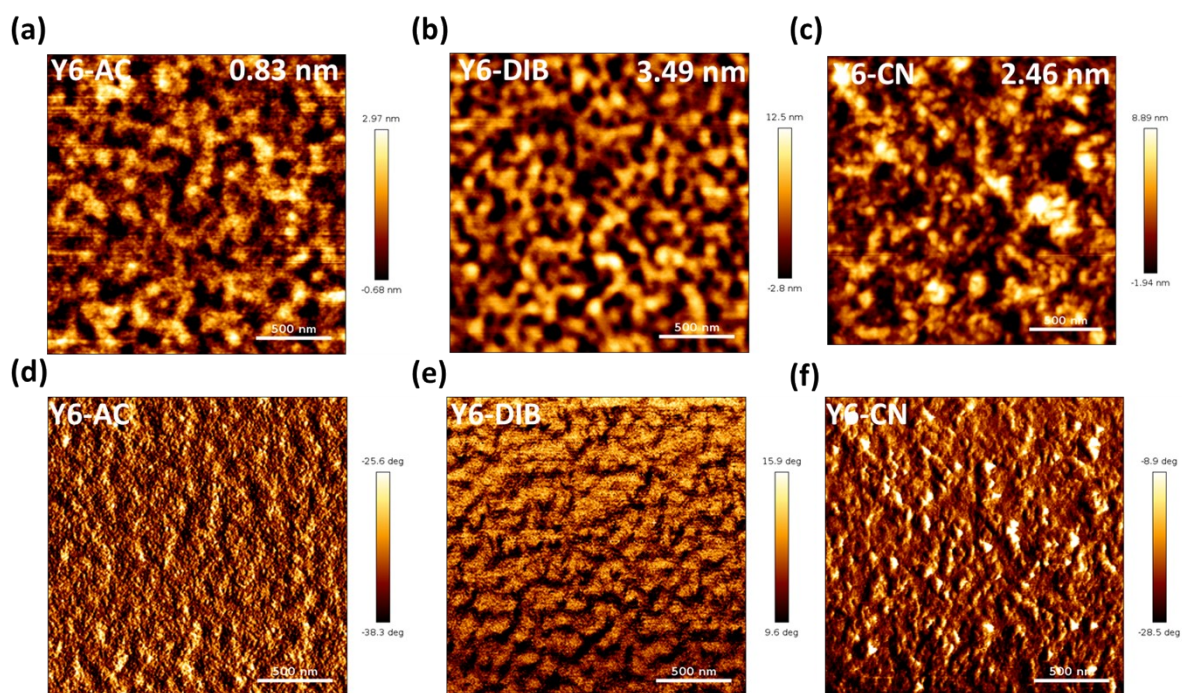


**Figure S22. a-c** Topography and **d-f** phase mappings of neat Y6 films processed under different conditions. The RMS variations of heights are labelled on the insets.
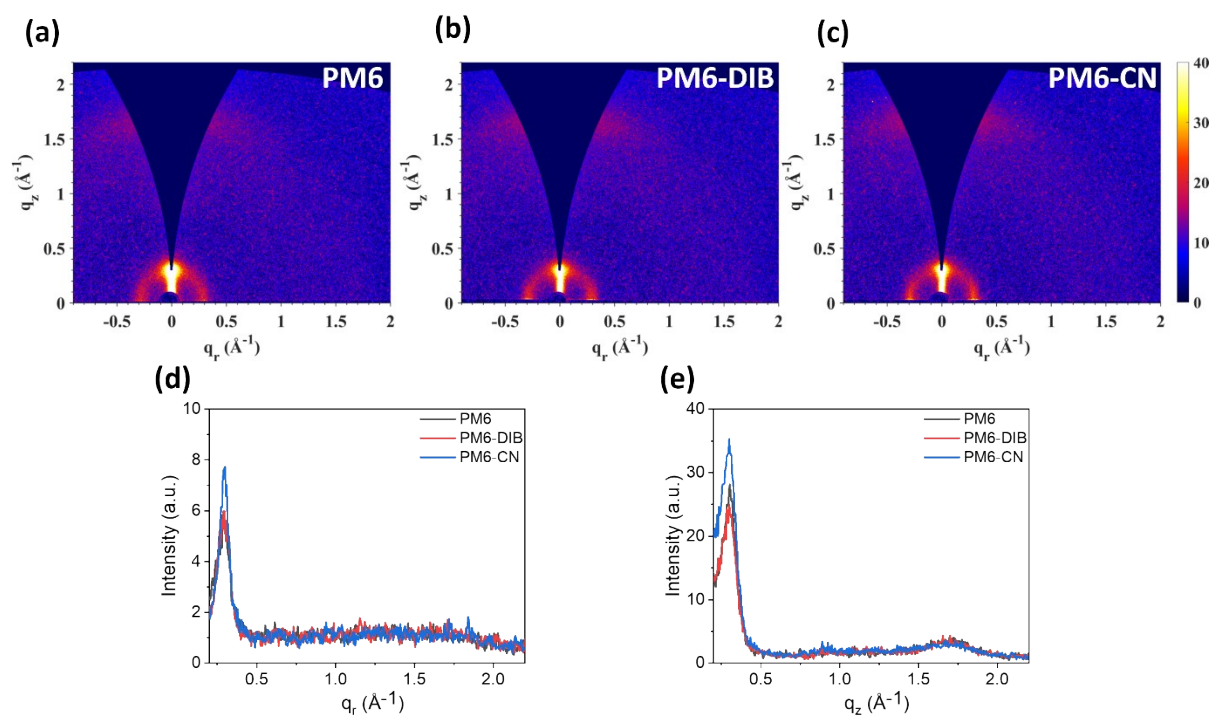
**Figure S23.** 2-D GIWAXS plots of PM6 neat films deposited from CF **a** without additive, with **b** DIB, and **c** CN. The corresponding linecuts along the in-plane and out-of-plane directions are shown in **d** and **e**, respectively. All films were thermally annealed at 100 °C to align with the condition applied for LBL blend films and devices.

**Figure S24.** Topography mappings of PM6 neat films deposited from CF without **a** additive, with **b** DIB, and **c** CN obtained using tapping-mode AFM. The RMS roughness for each film is labelled on the inset. The corresponding phase mappings are shown in **d-f**.
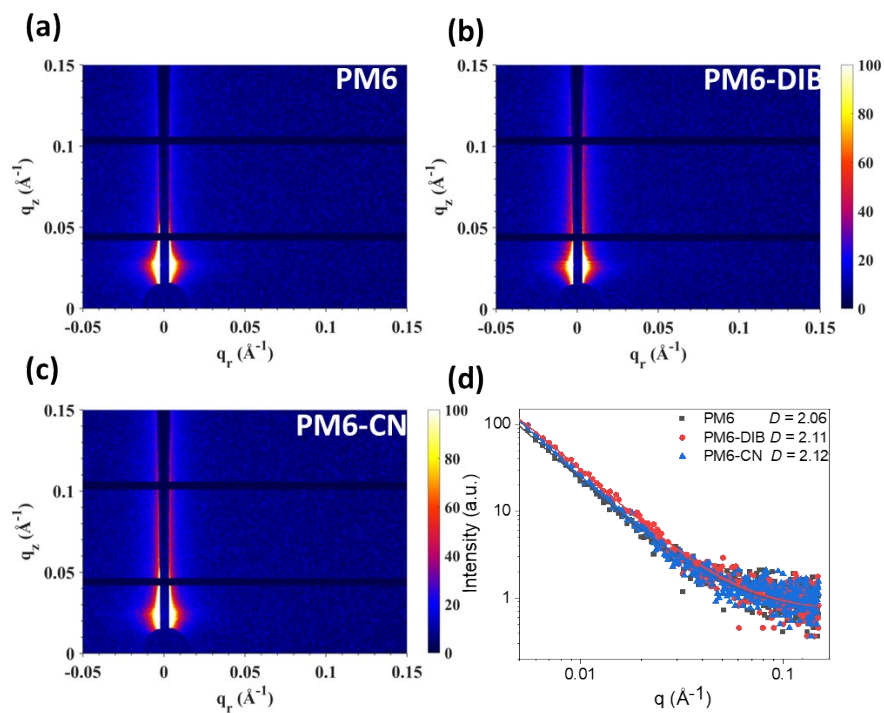


**Figure S25. a-c** 2-D GISAXS plots of neat PM6 films processed under different conditions. The in-
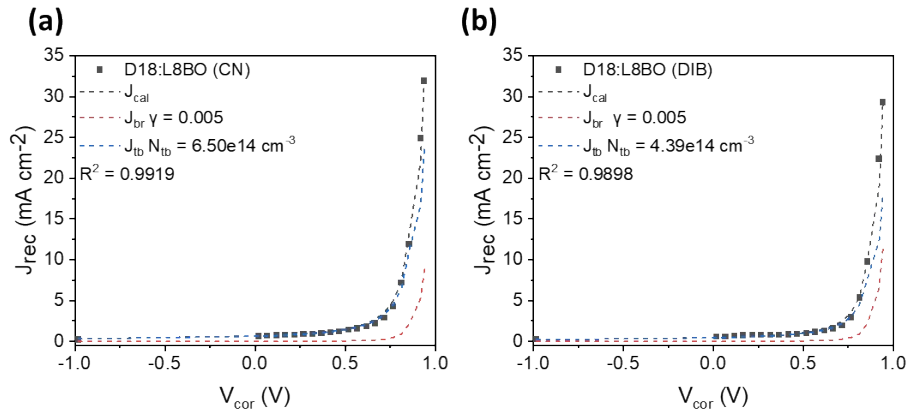
plane linecuts extracted at the Yoneda peak positions (dots) with their best fits (solid lines) are shown in **d**. Each linecut is fitted using a single fractal term with its fractal dimension (*D*) included in the legend.
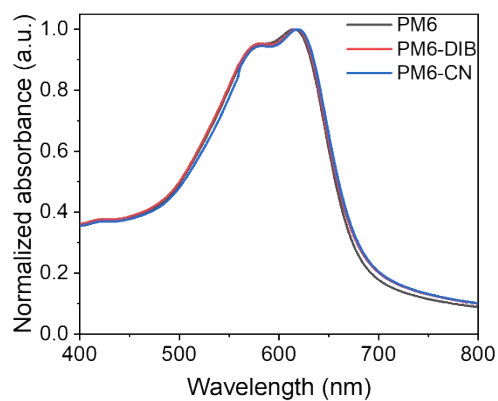


**Figure S26.** Normalized UV-Vis absorption spectra of PM6 neat films deposited from CF without additive, with DIB, and with CN.

**(a)**

**(b)**
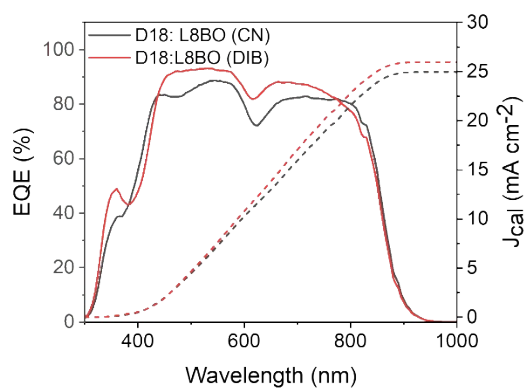
**Figure S28.** Recombination current fittings for D18:L8BO LBL devices with **a** CN and **b** DIB incorporated into the L8BO layer. The contribution from the bimolecular ($J_{br}$) and trap-assisted ($J_{tb}$) recombination currents are highlighted, along with the Langevin reduction factor ($\gamma$) and bulk trap density ($N_{tb}$) obtained from the fittings. The quality of the fitting is represented by $R^2$.



**(a)**          **(b)**

**(c)**          **(d)**
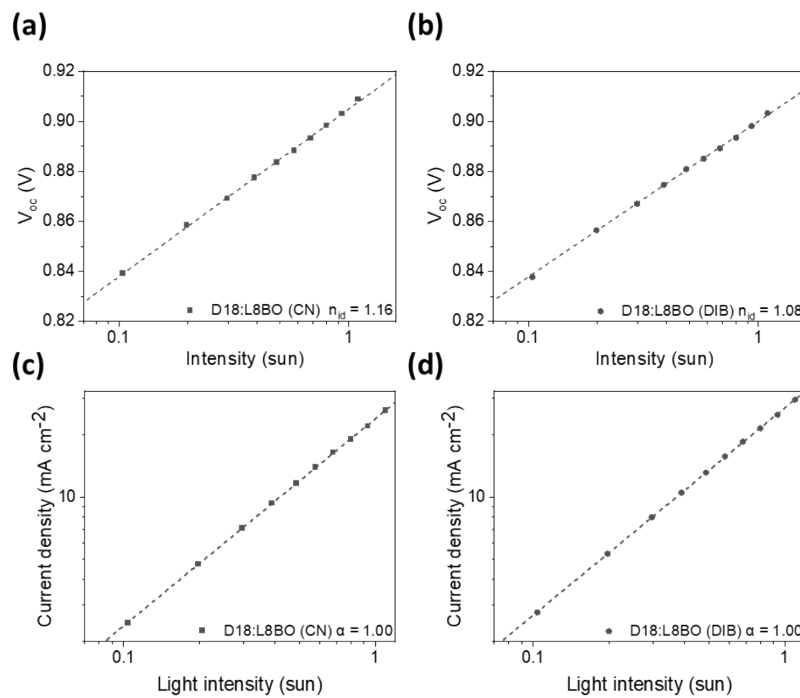
**Figure S29.** Light-intensity dependent **a-b** $J_{sc}$ and **c-d** $V_{oc}$ measurements on D18:L8BO LBL devices. For each device, the ideality factor ($n_{id}$) and power-law exponent ($\alpha$), extracted from the gradients of

*V*$_{oc}$ and *J*$_{sc}$, respectively, are shown in the insets.
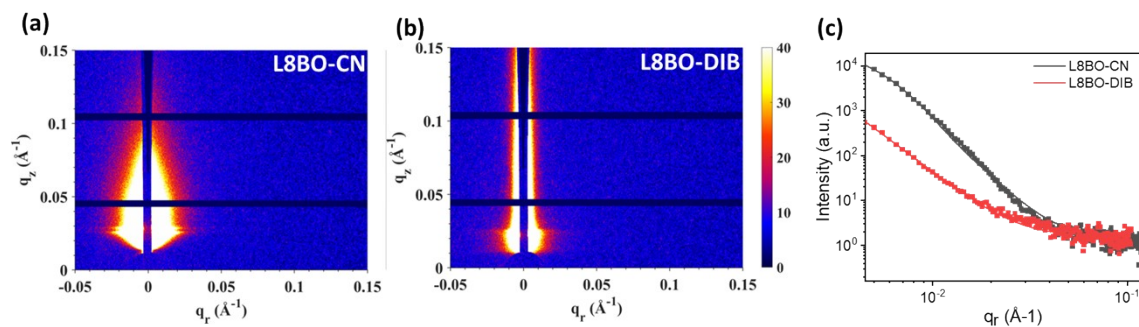


**Figure S30.** 2-D GISAXS plots of **a** L8BO-CN and **b** L8BO-DIB neat films with their in-plane linecuts (squares) and best fittings (solid lines) shown in **c**.
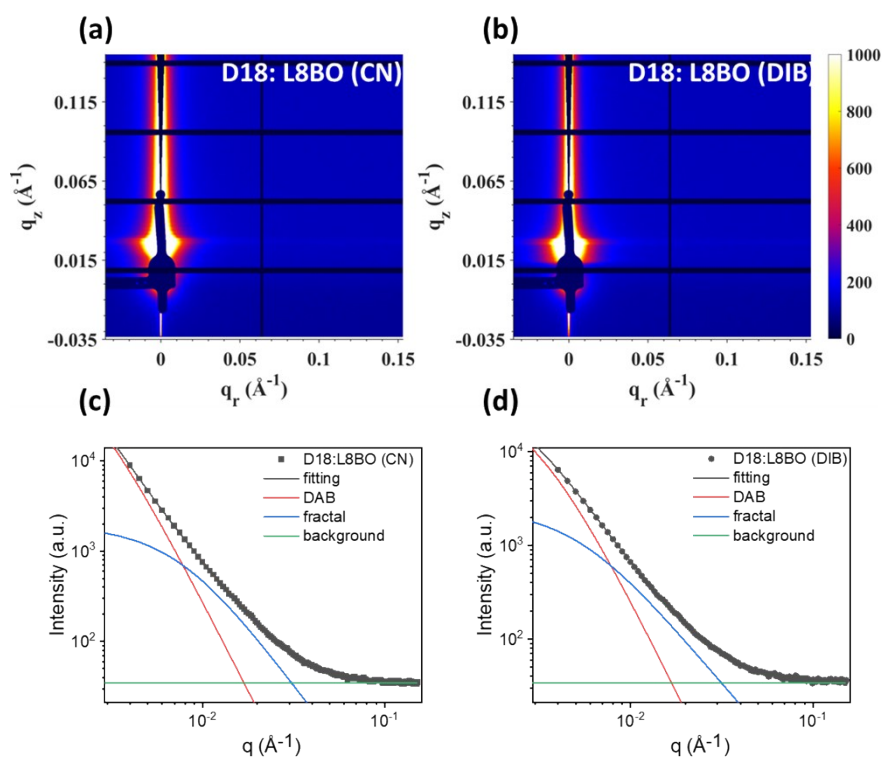


**Figure S31.** 2-D GISAXS plots of **a** D18: L8BO (CN) and **b** D18: L8BO (DIB) LBL films. Their in-plane linecuts (squares) and best fittings (solid lines) are shown in **c** and **d**, respectively.
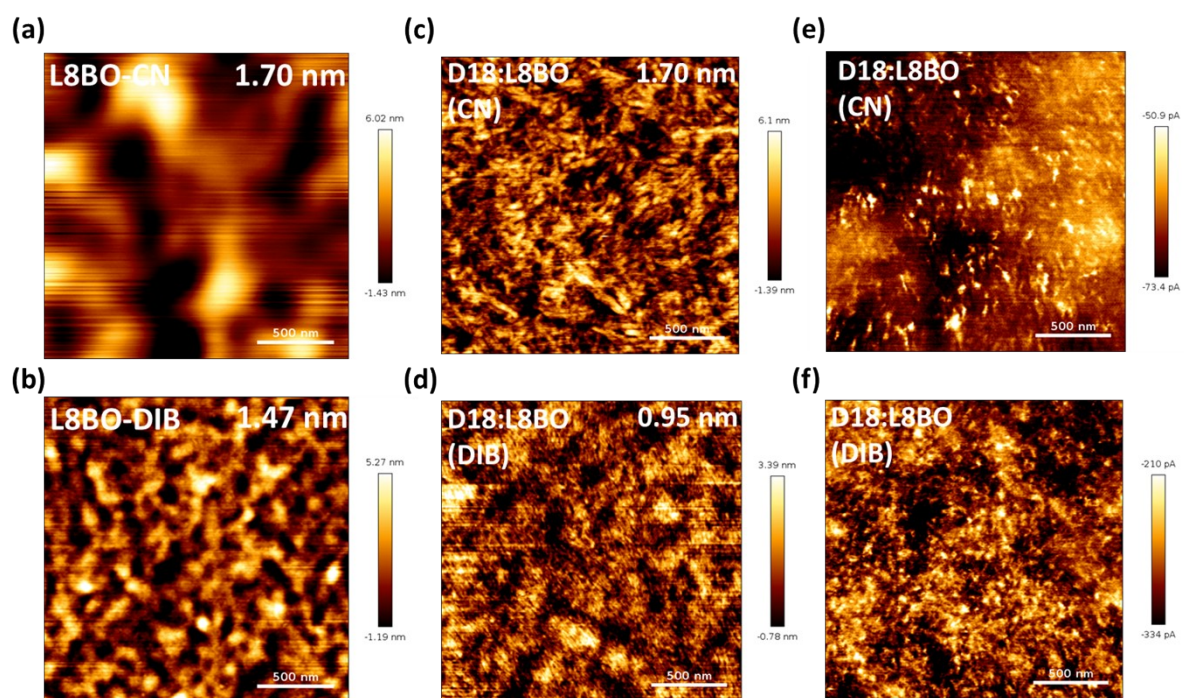
**Figure S32.** AFM topography mappings of **a** L8BO-CN and b L8BO-DIB neat films, and D18: L8BO LBL films with **c** CN and **d** DIB. The corresponding c-AFM mappings of LBL films are shown in **e** and **f**.

# Supplementary Tables

**Table S1** A summary of performances for PM6:Y6 devices before and after thermal annealing at 100 °C for 5 mins without incorporating any additive.

| Devices | $J_{sc}{}^a$ (mA cm$^{-2}$) | $FF^a$ (%) | $V_{oc}{}^a$ (V) | $PCE^a$ (%) | $\gamma$ | $N_{tb}$ (cm-3) |
|---|---|---|---|---|---|---|
| BHJ-AC$^b$ | 27.0 (26.9±0.2) | 72.2 (71.4±0.7) | 0.868 (0.864±0.003) | 16.9 (16.6±0.2) | 0.0125 | 6.2 × 10$^{14}$ |
| TA_5 mins | 28.6 (28.3±0.2) | 71.8 (71.5±0.5) | 0.850 (0.847±0.005) | 17.4 (17.1±0.3) | 0.0052 | 7.8 × 10$^{14}$ |

[a] Figures of merits for champion devices together with the average values and standard deviation (in parenthesis) obtained from 6-8 independent devices. [b] A new batch of BHJ-AC devices was fabricated to make a fair comparison.

**Table S2** A summary of active layer morphology for D18:L8BO LBL films with CN or DIB incorporated into the L8BO layer.

| Samples | $\xi$ (nm) | $2R_{gc}$(nm) | $D_f$ |
|---|---|---|---|
| D18:L8BO (CN) | 51.8 | 53.8 | 2.51 |
| D18:L8BO (DIB) | 36.8 | 74.4 | 2.25 |

# Supplementary References

1. M. J. Frisch, G. W. Trucks, H. B. Schlegel, G. E. Scuseria, M. A. Robb, J. R. Cheeseman, G. Scalmani, V. Barone, G. A. Petersson, H. Nakatsuji, X. Li, M. Caricato, A. V. Marenich, J. Bloino, B. G. Janesko, R. Gomperts, B. Mennucci, H. P. Hratchian, J. V. Ortiz, A. F. Izmaylov, J. L. Sonnenberg, Williams, F. Ding, F. Lipparini, F. Egidi, J. Goings, B. Peng, A. Petrone, T. Henderson, D. Ranasinghe, V. G. Zakrzewski, J. Gao, N. Rega, G. Zheng, W. Liang, M. Hada, M. Ehara, K. Toyota, R. Fukuda, J. Hasegawa, M. Ishida, T. Nakajima, Y. Honda, O. Kitao, H. Nakai, T. Vreven, K. Throssell, J. A. Montgomery Jr., J. E. Peralta, F. Ogliaro, M. J. Bearpark, J. J. Heyd, E. N. Brothers, K. N. Kudin, V. N. Staroverov, T. A. Keith, R. Kobayashi, J. Normand, K. Raghavachari, A. P. Rendell, J. C. Burant, S. S. Iyengar, J. Tomasi, M. Cossi, J. M. Millam, M. Klene, C. Adamo, R. Cammi, J. W. Ochterski, R. L. Martin, K. Morokuma, O. Farkas, J. B. Foresman and D. J. Fox, *Journal*, 2016.
2. A. D. McLean and G. S. Chandler, *The Journal of Chemical Physics*, 1980, **72**, 5639-5648.
3. M. L. Laury, M. J. Carlson and A. K. Wilson, *Journal of Computational Chemistry*, 2012, **33**, 2380-2387.
4. L. S. C. Pingree, O. G. Reid and D. S. Ginger, *Nano Letters*, 2009, **9**, 2946-2952.
5. O. Douhéret, L. Lutsen, A. Swinnen, M. Breselge, K. Vandewal, L. Goris and J. Manca, *Appl. Phys. Lett.*, 2006, **89**.
6. P. S. Fernando and J. M. Mativetsky, *The Journal of Physical Chemistry C*, 2023, **127**, 9903-9910.
7. W.-R. Wu, U. S. Jeng, C.-J. Su, K.-H. Wei, M.-S. Su, M.-Y. Chiu, C.-Y. Chen, W.-B. Su, C.-H. Su and A.-C. Su, *ACS Nano*, 2011, **5**, 6233-6243.
8. U.-S. Jeng, C. H. Su, C.-J. Su, K.-F. Liao, W.-T. Chuang, Y.-H. Lai, J.-W. Chang, Y.-J. Chen, Y.-S. Huang, M.-T. Lee, K.-L. Yu, J.-M. Lin, D.-G. Liu, C.-F. Chang, C.-Y. Liu, C.-H. Chang and K. S. Liang, *Journal of Applied Crystallography*, 2010, **43**, 110-121.
9. H.-C. Liao, C.-S. Tsao, T.-H. Lin, C.-M. Chuang, C.-Y. Chen, U. S. Jeng, C.-H. Su, Y.-F. Chen and W.-F. Su, *Journal of the American Chemical Society*, 2011, **133**, 13064-13073.
10. J. Mai, T.-K. Lau, J. Li, S.-H. Peng, C.-S. Hsu, U. S. Jeng, J. Zeng, N. Zhao, X. Xiao and X. Lu, *Chem. Mater.*, 2016, **28**, 6186-6195.
11. J. W. Kiel, A. P. R. Eberle and M. E. Mackay, *Physical Review Letters*, 2010, **105**, 168701.
12. V. V. Brus, *Semiconductor Science and Technology*, 2012, **27**, 035024.
13. V. V. Brus, C. M. Proctor, N. A. Ran and T.-Q. Nguyen, *Advanced Energy Materials*, 2016, **6**, 1502250.
14. J. Vollbrecht, V. V. Brus, S. J. Ko, J. Lee, A. Karki, D. X. Cao, K. Cho, G. C. Bazan and T. Q. Nguyen, *Advanced Energy Materials*, 2019, **9**, 1901438.
15. L. Q. Phuong, S. M. Hosseini, O. J. Sandberg, Y. Zou, H. Y. Woo, D. Neher and S. Shoaee, *Solar RRL*, 2021, **5**, 2000649.
16. Y. Xiao and X. Lu, *Materials Today Nano*, 2019, **5**, 100030.
17. A. Classen, C. L. Chochos, L. Lüer, V. G. Gregoriou, J. Wortmann, A. Osvet, K. Forberich, I. McCulloch, T. Heumüller and C. J. Brabec, *Nature Energy*, 2020, **5**, 711-719.
18. Z. Wang, Y. Guo, X. Liu, W. Shu, G. Han, K. Ding, S. Mukherjee, N. Zhang, H.-L. Yip, Y. Yi, H. Ade and P. C. Y. Chow, *Nature Communications*, 2024, **15**, 1212.

19.  Y. Firdaus, V. M. Le Corre, S. Karuthedath, W. Liu, A. Markina, W. Huang, S. Chattopadhyay, M. M. Nahid, M. I. Nugraha, Y. Lin, A. Seitkhan, A. Basu, W. Zhang, I. McCulloch, H. Ade, J. Labram, F. Laquai, D. Andrienko, L. J. A. Koster and T. D. Anthopoulos, *Nature Communications*, 2020, **11**, 5220.

20.  U. Rau, B. Blank, T. C. M. Müller and T. Kirchartz, *Physical Review Applied*, 2017, **7**, 044016.

21.  O. Almora, C. I. Cabrera, J. Garcia-Cerrillo, T. Kirchartz, U. Rau and C. J. Brabec, *Advanced Energy Materials*, 2021, **11**, 2100022.

22.  M. M. Mandoc, F. B. Kooistra, J. C. Hummelen, B. de Boer and P. W. M. Blom, *Applied Physics Letters*, 2007, **91**.

23.  S. Zeiske, W. Li, P. Meredith, A. Armin and O. J. Sandberg, *Cell Reports Physical Science*, 2022, **3**, 101096.

24.  X. Liao, M. Liu, H. Pei, P. Zhu, X. Xia, Z. Chen, Y. Zhang, Z. Wu, Y. Cui, G. Xu, M. Gao, L. Ye, R. Ma, T. Liu, X. Lu, H. Zhu and Y. Chen, *Angewandte Chemie International Edition*, 2024, **63**, e202318595.

25.  Z. Chen, X. Chen, B. Qiu, G. Zhou, Z. Jia, W. Tao, Y. Li, Y. M. Yang and H. Zhu, *The Journal of Physical Chemistry Letters*, 2020, **11**, 3226-3233.

26.  S.-i. Natsuda, T. Saito, R. Shirouchi, Y. Sakamoto, T. Takeyama, Y. Tamai and H. Ohkita, *Energy & Environmental Science*, 2022, **15**, 1545-1555.

27.  Y. Tamai, Y. Murata, S.-i. Natsuda and Y. Sakamoto, *Advanced Energy Materials*, 2024, **14**, 2301890.